ERDC/CRREL TR-18-13

US Army Corps
of Engineers®
Engineer Research and
Development Center

ERDC
ENGINEER RESEARCH & DEVELOPMENT CENTER

ERDC 6.2 Geospatial Research and Engineering (GRE) ARTEMIS STO-R DUST-CLOUD

A Comparison of Simulated Dust Produced by Three Dust-Emission Schemes in WRF-Chem

Case-Study Assessment

Theodore W. Letcher and Sandra L. LeGrand

August 2018

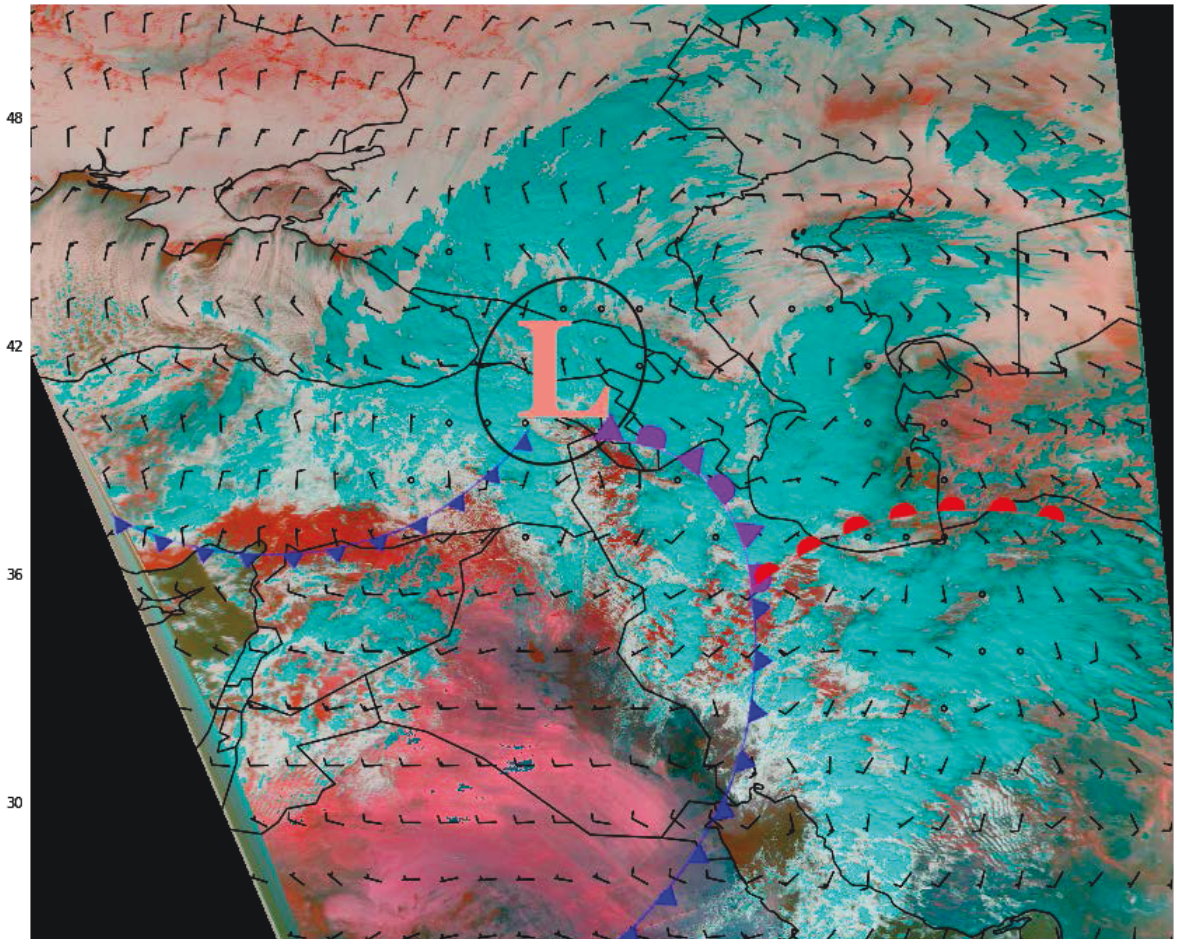

Cold Regions Research
and Engineering Laboratory

The U.S. Army Engineer Research and Development Center (ERDC) solves the nation's toughest engineering and environmental challenges. ERDC develops innovative solutions in civil and military engineering, geospatial sciences, water resources, and environmental sciences for the Army, the Department of Defense, civilian agencies, and our nation's public good. Find out more at www.erdc.usace.army.mil.

To search for other technical reports published by ERDC, visit the ERDC online library at http://acwc.sdp.sirsi.net/client/default.

ERDC/CRREL TR-18-13
August 2018

A Comparison of Simulated Dust Produced by Three Dust-Emission Schemes in WRF-Chem

Case-Study Assessment

Theodore W. Letcher and Sandra L. LeGrand

U.S. Army Engineer Research and Development Center (ERDC)
Cold Regions Research and Engineering Laboratory (CRREL)
72 Lyme Road
Hanover, NH 03755-1290

Final Report

Prepared for Assistant Secretary of the Army for Acquisition, Logistics, and Technology
103 Army Pentagon
Washington, DC 20314-1000

Under ERDC 6.2 Geospatial Research and Engineering (GRE) Army Terrestrial-Environmental modeling and Intelligence System Science Technology Objective—Research (ARTEMIS STO-R) 053HJ0/FAN U4357509, "Dynamic Undisturbed Soils Testbed to Characterize Local Origins and Uncertainties of Dust (DUST-CLOUD)"

Abstract

Airborne mineral dust is one of the main forms of atmospheric aerosols, influencing, among other things, global weather patterns, biogeochemical processes, air quality, sensor performance, and visibility conditions on the ground. This study evaluates three dust-emission parameterizations available in the widely used Weather Research and Forecast model: the GOCART (Global Ozone Chemistry Aerosol Radiation and Transport), AFWA (Air Force Weather Agency), and UoC (University of Cologne) dust-emission schemes. The simulations were performed for a dust event that occurred over the Arabian Peninsula on 25 January 2010. The simulations were able to adequately reproduce the meteorological conditions of the event, and all three dust-emission schemes produced a dust event over the Arabian Peninsula. However, there were large differences in magnitude and extent between the three emissions schemes. Of the three schemes evaluated here, the AFWA scheme most closely matched the observed dust plume. Analysis revealed that differences between the schemes could largely be traced to differences in how each calculate the threshold wind speed (i.e., the minimum wind speed required for dust to be lofted).

Contents

Figures and Tables

Figures

Tables

Preface

This study was conducted for the Assistant Secretary of the Army for Acquisition, Logistics, and Technology under the U.S. Army Engineer Research and Development Center (ERDC) 6.2 Geospatial Research and Engineering (GRE) Applied Research Program Army Terrestrial Environmental Modeling and Intelligence System Science Technology Objective—Research (ARTEMIS STO-R) 053HJ0/FAN U4357509, "Dynamic Undisturbed Soils Testbed to Characterize Local Origins and Uncertainties of Dust (DUST-CLOUD)." The ARTEMIS technical program monitor was Mr. John Eylander, CEERD-RR.

The work was performed by the Terrestrial and Cryospheric Sciences Branch (CEERD-RRG) of the Research and Engineering Division (CEERD-RR), ERDC Cold Regions Research and Engineering Laboratory (CRREL). At the time of publication, Dr. John W. Weatherly was Chief, CEERD-RRG, and Mr. J. D. Horne was Chief, CEERD-RR. The Deputy Director of ERDC-CRREL was Mr. David B. Ringelberg, and the Director was Dr. Joseph L. Corriveau.

COL Ivan P. Beckman was the Commander of ERDC, and Dr. David W. Pittman was the Director.

Acronyms and Abbreviations

AFWA	Air Force Weather Agency
AOD	Aerosol Optical Depth
ARTEMIS	Army Terrestrial Environmental Modeling and Intelligence System
CFSR	Climate Forecast System Reanalysis
CRREL	Cold Regions Research and Engineering Laboratory
DUST-CLOUD	Dynamic Undisturbed Soils Testbed to Characterize Local Origins and Uncertainties of Dust
ERDC	U.S. Army Engineer Research and Development Center
FROPA	Frontal Passage
GOCART	Global Ozone Chemistry Aerosol Radiation and Transport
GRE	Geospatial Research and Engineering
MODIS	Moderate Resolution Imaging Spectroradiometer
NWP	Numerical Weather Prediction
RRTMG	Rapid Radiative Transfer Model for General Circulation Models
STO-R	Science Technology Objective—Research
UoC	University of Cologne
UTC	Coordinated Universal Time
WRF-Chem	Weather Research and Forecasting Chemistry

1 Introduction

1.1 Background

Airborne mineral dust is one of the main forms of atmospheric aerosol and is especially concentrated over the world's desert regions (Prospero et al. 2002). It influences global weather, climate patterns, and biogeochemical processes on many different spatial and temporal scales (e.g., Mahowald et al. 2005, 2010, 2014; Ravi et al. 2011; Webb et al. 2012; Boucher et al. 2013; Wang et al. 2017). Furthermore, hazardous air quality conditions created by dust can adversely affect agriculture, equipment performance, visibility, and human health at regional and local scales (e.g., Rushing et al. 2005; De Longueville et al. 2010; Okin et al. 2011; Sprigg et al. 2014; Middleton 2017; Al-Hemoud et al. 2017). As a result, atmospheric dust simulation and prediction model development is a priority for the research, operational forecasting, military, and hazard-prevention communities (Knippertz and Stuut 2014; Sprigg et al. 2014; Shepherd et al. 2016).

Wind-driven dust entrainment primarily occurs through a process called *saltation*, in which wind-lofted sand grains or aggregates too heavy to remain suspended in the air collide with the land surface and eject smaller "dust-sized" particles upon impact (e.g., Kok et al. 2012). Accurately representing saltation and dust-emission patterns in numerical weather prediction (NWP) models continues to be a challenge, largely because these phenomena are affected by difficult-to-obtain land surface attributes (e.g., soil texture and particle size distribution, degree of surface crusting, surface roughness, etc.) and momentum transfer processes that occur over a range of global to microscales (Richter and Gill 2018).

All modern NWP models incorporate simplified or idealized representations of physical processes and environmental attributes called *parameterizations* to account for subgrid scale, overly complex, or difficult-to-characterize phenomena. These parameterizations prescribe values or relate processes to other known factors to retain the "essential aspects" of the process or feature they are designed to represent. However, the designation of "essential" may be relative to a specific application or region of interest (i.e., simplifications appropriate for one application may not be vi-

able for another). As such, many NWP models are designed to be configurable with different parameterization options for simulating a diverse range of weather scenarios and environmental conditions.

Numerous dust-emission parameterization schemes (referred to as dust-emission schemes henceforth) have been developed for forecasting and research purposes over the past several decades (e.g., Tegen and Fung 1994; Marticorena and Bergametti 1995; Woodward 2001; Ginoux et al. 2001, 2004; Nickovic et al. 2001; Shao 2001; Liu et al. 2003, 2007 ; Kok et al. 2014). Understanding how these dust-emission schemes perform in various environmental scenarios is important for anyone interested in using NWP dust modeling tools for informed decision-making. To date, several dust simulation case-study assessments have been published (e.g., Cavazos et al. 2009; Shao 2007, 2011; Kumar et al. 2014 ; Rizza et al. 2017); however, most of these communications discuss relatively coarse, global-scale scenarios or simulations of strong wind events over prolific dust-source regions.

1.2 Objective

The primary purpose of this report is to document the ability of three broadly adopted dust-emission schemes to reproduce a winter dust event in Southwest Asia, a scenario where terrain state and prevailing weather patterns are primed to increase the overall likelihood of dusty conditions (e.g., 14th Operational Weather Squadron 2017a, 2017b).

1.3 Approach

For this study, we used the Weather Research and Forecasting Chemistry (WRF-Chem) modeling framework to compare the performance of three different dust-emission schemes currently available in WRF-Chem. WRF-Chem is an open-source, regional-scale NWP model capable of simulating atmospheric chemistry processes and aerosol transport simultaneously with other meteorological and land surface fields (Grell et al. 2005; Peckham et al. 2011). The three dust schemes documented in this report include (1) the dust-emission scheme from the Georgia Institute of Technology–Goddard Global Ozone Chemistry Aerosol Radiation and Transport (GOCART) atmospheric aerosol and chemistry model (Chin et al. 2000; dust scheme originally described by Ginoux et al. [2001, 2004]), (2) the Air Force Weather Agency (AFWA) scheme (Jones 2012), and (3) the University of Cologne (UoC) scheme described by Shao (2001, 2004)

and Shao et al. (2011). Exact results from this case study are limited to our specific configuration of WRF-Chem; however, the findings may offer insight into how use of these schemes could affect simulation accuracy in other dust-modeling, visibility, or air-quality NWP capabilities.

2 Overview of Dust-Emission Schemes

It is important to note that the following descriptions are for the dust schemes as they are implemented within the WRF-Chem model and that the implementation of these schemes varies slightly when used in other models.

The WRF-Chem GOCART, AFWA, and UoC dust-emission schemes (as of WRF-Chem version 3.8) share some commonalities. For example, all three schemes compute dust-emission flux as a function of wind energy and soil properties (such as soil moisture and particle size) and incorporate a preferential dust-source parameter designed to represent the availability of loose, erodible soil particles. All three schemes also assume that dust emissions are the result of saltation initiated when wind energies exceed critical thresholds. Each scheme divides emitted dust particles into five size-based groupings called *size bins*. These size bins follow a 1.46 μm, 2.8 μm, 4.8 μm, 9 μm, and 16 μm effective particle diameter size distribution configuration. Once injected into the lowest atmospheric model level, separate transport, removal, and radiative transfer schemes are used to estimate simulated atmospheric dust mass concentrations and optical properties.

2.1.1 GOCART dust-emission scheme

Dust-emission flux values (F_p, kg m^{-2} s^{-1}) for each size bin (D_p, cm) are calculated in the GOCART scheme using

$$F_p(D_p) = \begin{cases} CSs_p U^2 \left(U - U_t(D_p, \theta_s)\right), & U > U_t(D_p, \theta_s) \\ 0, & U \le U_t(D_p, \theta_s) \end{cases}, \quad (1)$$

where

C = a dimensional proportionality constant (default set to 0.8 × 10^9 kg s^2 m^{-5}),
S = a unitless dust-source strength function indicating availability of loftable dust material,
s_p = the mass fraction of emitted dust for the soil separate class (i.e., sand, silt, or clay) of size group p,
U = the horizontal wind speed at 10 m above ground level (m s^{-1}),
θ_s = soil moisture degree of saturation, and

$U_t(D_p, \theta_s)$ = the threshold 10 m wind speed required for initiating erosion (m s^{-1}).

The threshold wind speed (U_t, m s^{-1}) was derived for dry soil based on particle diameter following

$$U_t(D_p) = 0.13c \frac{\left(\frac{\sqrt{\rho_s g D_p}}{\rho_a}\right)\left(\sqrt{1+\frac{0.006}{\rho_s g D_p^{2.5}}}\right)}{\sqrt{1.928*\left[1331.0*D_p^{1.56}+0.38\right]^{0.092}-1.0}} \quad (2)$$

and adjusted for soil moisture

$$U_t(D_p, \theta_s) = U_t(D_p) * (1.2 + 0.2 * \log_{10}[\theta_s]), \quad (3)$$

where

ρ_a = the air density (g cm^{-3}),
ρ_s = the particle density (constant at 2.65 g cm^{-3}),
g = the gravitational constant (981 cm s^{-2}), and
c = a dimensional constant for converting the final value from centimeters to meters (0.01 m cm^{-1}).

From equations (1)–(3), it is apparent that wind speed, soil moisture, and air density (which are provided by WRF-Chem) are the only necessary variable inputs for the calculation of F_p. The S term is a time-static, spatially variable field diagnosed from quarter-degree resolution terrain elevation data in the model preprocessor via

$$S = ((z_{max} - z_i)/(z_{max} - z_{min}))^5, \quad (4)$$

where z_i is the elevation of a given location, and z_{max} and z_{min} are the maximum and minimum elevations of the surrounding terrain within a 10° × 10° area. Resultant values for S are set to zero anywhere bare soil is not indicated by data derived from the Advanced Very High Resolution Radiometer product (DeFries and Townshend 1994) and interpolated to the model grid. All other terms in the F_p calculation are prescribed.

Of note, the GOCART equation for U_t has been modified several times over the years, and these changes are incompletely documented in the litera-

ture. In WRF-Chem, U_t is calculated using a semiempirical function derived in terms of friction velocity, u_*, a parameter used to represent wind-shear stress based on changes in wind speed with height, surface roughness, and atmospheric stability. Although values of u^* and U are both expressed in dimensions of speed, they are not equivalent and generally differ by one or more orders of magnitude. This error leads to almost universally overestimated dust emission due to very low-magnitude values of U_t and the exponential aspect of the dust flux calculation. Typically, these errors are adjusted to be more realistic by using tuning constants to scale F_p.

2.1.2 AFWA dust-emission scheme

The AFWA scheme is a modified version of the scheme originally described by Marticorena and Bergametti (1995). A Bulk vertical dust flux (F) is determined by summing dust emission fluxes caused by saltating particles over nine saltation size particle bins ranging from 0.7 to 125 μm in diameter:

$$F = \sum_{i=1}^{9} F_i(D_s),$$

where D_s is the diameter of the saltation particle and i is the saltation particle bin. F_i is determined using a semiempirical u_*-based function, a dust-source strength function, and soil texture via

$$F_i = \begin{cases} \beta S Q_{D_s}, & u_* > u_{*t}(D_s, \theta_g) \\ 0, & u_* \le u_{*t}(D_s, \theta_g) \end{cases}, \quad (5)$$

where

β = the sandblasting efficiency;
Q_{D_s} = the saltation flux for particles of size D_s; and
u_{*t} = the threshold friction velocity required for dust-lofting initiation based on D_s and gravimetric soil moisture, θ_g.

Q_{D_s} is calculated by

$$Q_{D_s} = c\frac{\rho}{g}u_*^3\left(1 - \frac{u_{*,t(D_s)}}{u_*}\right)\left(1 + \left[\frac{u_{*,t(D_s)}}{u_*}\right]^2\right), \quad (6)$$

where

c = an empirical proportionality constant (default set to 1.0),
ρ_a = air density, and
g = the gravitational acceleration constant.

Notably, the initial threshold friction velocity U_T is calculated using equation (2) though the soil moisture correction factor is calculated differently than in GOCART, using a modified version of the correction function described by Fécan et al. (1998):

$$f(\theta_g) = \begin{cases} \sqrt{1 + A(\theta_g - \theta_g{}')^b}, & \theta_g > \theta_g{}' \\ 1, & \theta_g \leq \theta_g{}' \end{cases} \quad (7)$$

where

$\theta_g{}'$ = the gravimetric soil moisture,
$\theta_g{}'$ = the minimum soil moisture threshold required to activate the soil moisture correction, and
A and b = constants determined by the WRF-Chem soil category.

A key difference with respect to how the dust emission flux (*F)* is calculated between the GOCART and AFWA emissions schemes is that in AFWA, a bulk vertical dust flux is calculated and then distributed into the suspended dust size bins described at the beginning of section 2, following the Kok (2011) brittle fragmentation theory, whereas in GOCART, *F* is calculated separately for each of the five dust bins based on a U_T calculated for each size bin.

2.1.3 UoC dust-emission scheme

The UoC scheme is based on the work of Shao (2001, 2004) and Shao et al. (2011). It essentially provides the user with three versions of the Shao dust scheme (noted as S01, S04, and S11, respectively, in order of increasing simplification). While the three UoC scheme settings could be considered the most physically based dust-emission scheme options in the WRF-Chem framework, the underlying physics require sophisticated knowledge of soil characteristics that are largely prescribed in most NWP models. This report focuses on the S04 option since it incorporates physically

based aggregate disintegration algorithms not included in the S11 setting but has less dependency on soil attributes than S01.

Size-resolved dust-emission flux is calculated by,

$$\begin{cases} F(D_p, D_s) = c_y \eta_f [(1-\gamma) + \gamma \sigma_p](1+\sigma_m) g \left(\frac{Q_{D_S}}{{u_*}^2}\right), & u_* > u_{*t}(D_s, \theta_v, \dots) \\ F(D_p, D_s) = 0, & u_* \le u_{*t}(D_s, \theta_v, \dots) \end{cases}, \quad (8)$$

where

c_y = a dimensionless coefficient (default set to 1×10^{-4}),
η_f = the fraction of emitted dust that can be injected into the first model level and is a function of particle diameter,
σ_p = the ratio between the fraction of free dust and that of aggregated dust,
σ_m = the bombardment efficiency,
Q_{D_s} = the saltation flux for particles of size D_s,
θ_v = the volumetric soil moisture, and
γ = a function that describes the binding strength of aggregated dust.

Q_{D_s} is calculated following

$$Q_{D_s} = (1-c_f) 2.3 \frac{\rho}{g} u_*^3 \left(1 - \frac{u_{*,t}(D_S, \theta_v, c_f)}{u_*}\right)\left(1 + \left[\frac{u_{*,t}(D_S, \theta_v, c_f)}{u_*}\right]^2\right), \quad (9)$$

where the threshold friction velocity, $u_{*,t}(D_s, \theta_v, c_f)$, is determined via a function similar to the one used in the AFWA scheme and is based on saltation particle size (D_s) and volumetric soil moisture (θ_v) but with additional corrections for surface drag effects based on the fraction of vegetation within the model gridcell (c_f). Note that the $(1-c_f)$ on the left-hand side of equation (9) is a vegetation-based surface-drag scaling factor that is in addition to the roughness correction applied to $u_{*,t}$.

3 Data and Methods

To evaluate the WRF-Chem simulated meteorology, we used surface weather station observations, atmospheric vertical profiles gathered from radiosondes, and reanalysis data. Because of the sparse data availability in the WRF-Chem domain, we chose not to perform a robust statistical validation of the model but rather a general evaluation of the case-study simulation to ensure that any errors in modelled dust concentrations were not primarily due to errors in simulated wind flow.

Evaluating simulated dust emissions can be challenging because comprehensive in situ dust-emission flux measurements are difficult to acquire (e.g., Shinoda et al. 2011; Webb et al. 2016) and remote-sensing techniques often struggle to discern elevated dust from the underlying background near emitting sources (e.g., Walker et al. 2009). Because of this general lack of dust-emission observations, we chose to assess the accuracy of simulated visibility near the land surface as an alternative since visibility is strongly influenced by dust in desert regions. Furthermore, near-surface visibility is regularly monitored by automated weather stations and has previously been used as a proxy for dust activity assessment in data-sparse areas (e.g., Mahowald et al. 2007; Shao et al. 2007; Westphal et al. 2009; Cavazos et al. 2009). We also visually compared simulated cloud cover and aerosol optical depth (AOD) diagnostics to dust-enhanced imagery for qualitative assessment of the simulated dust plume for this event.

3.1 The WRF-Chem model

Simulations for our assessment were performed using WRF-Chem version 3.8. Figure 1 shows the model domain. Each event simulation used a horizontal grid spacing of 12 km (484 × 417 grid points) and 48 terrain-following, vertical atmospheric levels set using a stretched sigma-coordinate system to favor higher vertical resolution near the land surface. Model data were produced for a 5-day period extending from 22 January 2010 0000 UTC (Coordinated Universal Time) to 27 January 2010 0000 UTC. Lateral boundary and initial model conditions were extracted from 1-degree, 6-hourly Global Forecast System final analysis reanalysis data (National Centers for Environmental Prediction et al. 2000). Simulations were initialized using a “cold start” technique, in which atmospheric dust concentrations begin at zero and output from the beginning of the simulation is discarded to enable adequate time for background dust generation and for

the model to remove any spurious features created by the initialization data. A 36-hour spin-up was selected based on a subjective assessment of a selection of meteorological and dust variables, including, for example, mean sea-level pressure, vertically integrated dust mass, and temperature at approximately 1500 m above sea level at 12, 24, 36, and 48 hours into the simulation. Findings from this review suggest that further increasing the spin-up time to 48 hours offered little benefit.

Figure 1. The top panel shows the WRF-Chem domain outlined in *black*. The marked locations show the surface meteorological stations (*red dots*) and radiosonde observations (*black stars*) used to evaluate the model. Zoomed in panels of the analysis region show model surface elevation (km) (*lower right*) and dust erodibility source function (*lower left*).

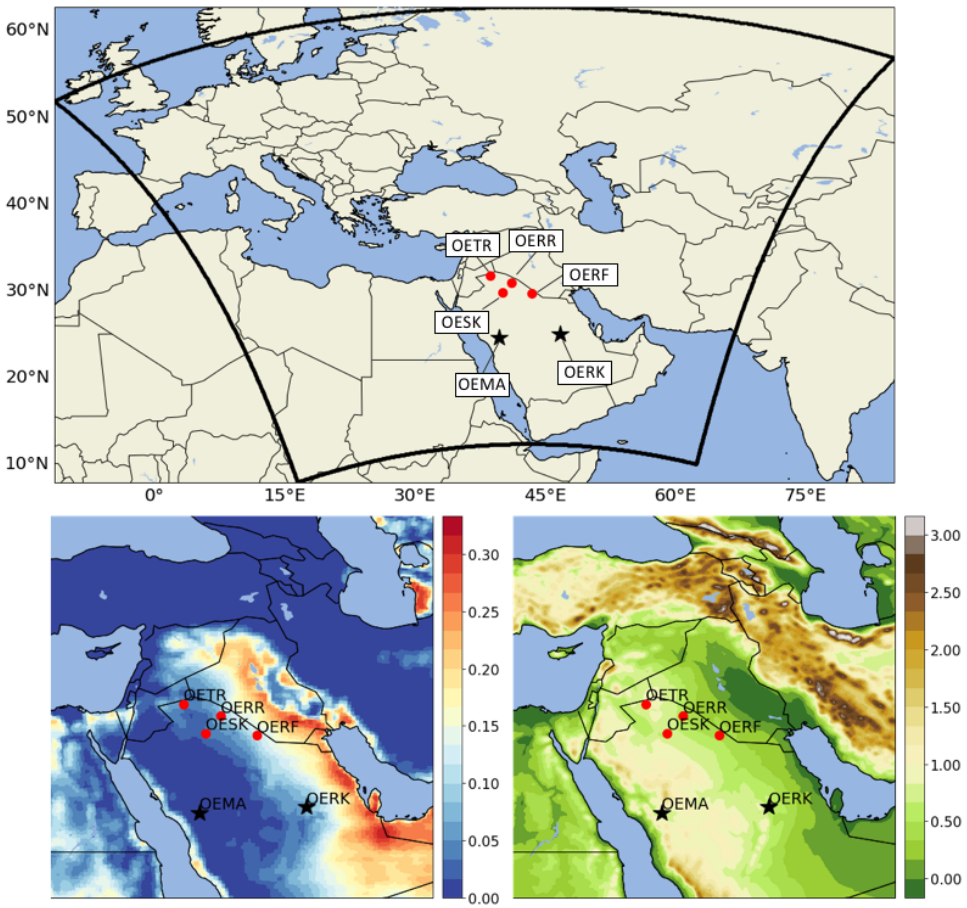

We generated additional atmospheric aerosol and gas phase chemistry fields by using a simplified version of the GOCART chemistry and aerosol module in WRF-Chem (chem_opt = GOCART_SIMPLE in the WRF-Chem configuration file). This enables the model to incorporate the effects of sea

salt, black carbon, organic carbon, sulfate, and dimethyl sulfide on total atmospheric aerosol loads. While the sea salt emissions are based on lowest model-level wind speeds over the oceans, the other background aerosol emissions were prescribed using climatological emissions data and the PREP-CHEM-SRC program (software designed for preprocessing WRF-Chem datasets, Freitas et al. [2011]).

Table 1 presents a full accounting of our model chemistry and physics parameterizations for subgrid-scale processes. Importantly, the aerosol cloud and radiative feedback options are turned off, which means that aerosol concentrations did not affect the evolution of other model fields and that weather conditions (e.g., wind speeds, turbulence, soil moisture, etc.) were identical across all simulations.

Table 1. WRF-Chem namelist configuration used in the WRF simulations.

WRF-Chem Parameterization	Scheme	Namelist Variable	Option
Cumulus	Kain-Fritsch	cu_physics	1
Land Surface Model	Noah v3.8	sf_surface_physics	2
Surface Layer	Monin-Obukhov	sf_sfclay_physics	1
Boundary Layer	MM5 2.5	bl_pbl_physics	5
Radiation (Shortwave and Longwave)	Rapid Radiative Transfer Model for General Circulation Models (RRTMG)	ra_sw(lw)_physics	4
Microphysics	Thompson	mp_physics	8
Chemistry	GOCART Simple	chem_opt	301
Background Emissions	GOCART Simple	emiss_opt	5
Aerosol Optics	Maxwell Approximation	aer_op_opt	2

3.2 Observations

To evaluate the simulated meteorology, a collection of available in situ data from automated surface meteorological weather stations and radiosonde observations in combination with gridded reanalysis data from the Climate Forecast System Reanalysis product (CFSR) was used. Surface meteorological and radiosonde observation locations are indicated, respectively, as red dots and black stars in Figure 1.

The surface observations (available at http://weather.uwyo.edu/surface/) used in this study provide hourly temperature, wind, humidity, and visibility measurements. Observational datasets from stations that were manned by

human observers also included present weather conditions. For example, datasets from human-monitored stations occasionally included symbols for "blowing dust" if a dust event was occurring in the vicinity at the time of the observation.

Radiosonde observations (available at http://weather.uwyo.edu/upperair/) are collected twice daily worldwide via weather balloon launches at 0000 and 1200 UTC. These observations provide high-quality in situ atmospheric profiles of temperature, wind, and humidity and were used to evaluate modelled atmospheric structure and vertical wind profiles at two locations within the domain near the dust event. These observations were visualized using Skew-T log-P diagrams, a common plotting convention used in meteorology to analyze the vertical structure of the atmosphere.

While in situ observations are ideal for assessing model accuracy, they are relatively sparse in both space and time over our region of interest. To supplement these observations, we also used half-degree, 6-hourly CFSR data (Saha et al. 2010b) to help evaluate how well the various WRF-Chem model configurations captured the overall evolution of our case-study dust event. Saha et al. (2010a) provides a full description of the CFSR product. Though reanalysis data are good for comparison purposes, it is important to remember that these datasets are a blend of observations and model output and thus cannot be considered truth. Rather, they provide a probable state of the atmosphere and offer useful discussion points for data-limited simulation assessments.

Taken together, the aforementioned data collections provide a good basis for evaluating simulated atmospheric states against the real atmosphere. However, these observations provide almost no information regarding atmospheric dust concentrations (only surface visibility measurements used as a proxy for dust concentrations provide this information). Therefore, to qualitatively assess spatial dust concentrations, dust-enhanced satellite-imagery derived from Moderate Resolution Imaging Spectroradiometer (MODIS) data using a processing algorithm by Miller (2003) was used (see Sinclair and Jones [2017] for the python script we used to generate dust-enhanced imagery in GeoTiff format). In the Miller (2003) technique, atmospheric dust is distinguished from the underlying background terrain using visible, near infrared, thermal infrared, and water vapor channels. Lofted dust appears pink, landscapes have blue and green hues,

water and steep terrain are red, and clouds appear aqua or cyan in the resulting image (e.g., cover image).

3.3 Simulation parameters of interest

As in most NWP models, WRF-Chem is designed to output standard meteorological fields like temperature, vertical and horizontal wind velocities, and mixing ratios of different water phases and hydrometeor species (e.g., snow) at multiple vertical levels. However, additional parameters of interest were needed to complete the assessment. The following section provides an overview of how AOD, cloud cover, and surface visibility were computed from model output data.

3.3.1 Aerosol optical depth (AOD)

WRF-Chem outputs simulated extinction coefficients for a select series of electromagnetic frequencies. These values have units of inverse length (e.g., m^{-1}) and represent signal attenuation caused by atmospheric particulates (e.g., dust and smoke), hydrometeors (e.g., rain, snow, and cloud droplets), and atmospheric gases. Here, we used total column AOD, which is calculated by vertically integrating extinction coefficients for a given frequency throughout an atmospheric column, as a means for representing atmospheric dust in desert regions. In this study, simulated 550 nm frequency (i.e., yellow visible light) extinction coefficients were vertically integrated to produce two-dimensional AOD fields:

$$AOD = \sum_{k=1}^{n_k} \mu_{550,k} \Delta z_k,$$

where

k = the model vertical level,
μ_{550} = the extinction coefficient at 550 nm, and
Δz = the physical depth of each vertical level.

3.3.2 Qualitative cloud cover

To diagnose simulated cloud cover (*CLD*), for qualitative comparison against satellite imagery, the simulated cloud- and ice-water mixing ratios were summed along the vertical dimension:

$$CLD = \sum_{k=1}^{n_k} CMR_k + 10xIMR_k,$$

where *CMR* and *IMR* are the cloud- and ice-water mixing ratios. In the above diagnostic, we chose to multiply *IMR* by a factor of 10 because *IMR* is generally at least an order of magnitude lower than the *CMR* and because ice clouds exhibit a relatively bright appearance in the dust-enhanced satellite imagery. This somewhat arbitrary scaling factor is justifiable in this instance since the variable *CLD* is used only for qualitative spatial comparison purposes and not quantitative evaluation.

3.3.3 Visibility

Visibility estimates were diagnosed from WRF-Chem data using 550 nm extinction coefficients and the Koschmieder visibility equation (Horvath 1971),

$$Vis = k\frac{3.912}{Ext_{550nm}},$$

where Ext_{550nm} is the average 550 nm extinction coefficient of the lowest three model levels and k is a factor equal to 0.6213 for converting kilometers to statute miles. These simulated visibilities were evaluated against surface visibility observations at the four surface stations shown in Figure 1.

4 Results

4.1 25 January 2010 dust-event overview

While dust was present over the analysis region throughout much of the case-study period, the primary focus was on the dust event that occurred between 0600 UTC on 25 January 2010 and 0000 UTC on 26 January 2010. This dust event followed a classic wintertime Shamal pattern (Figure 2) in which a cold front swept across the Arabian Peninsula, allowing a high-pressure cell to build in from the northwest and strengthen across Saudi Arabia. These atmospheric transitions forced strong northwesterly surface winds to blow across the region and loft large quantities of dust into the atmosphere.

Figure 2. Schematic showing the general meteorological configuration of a Shamal event. The map indicates the locations of the relevant high- and low-pressure centers. The *black dashed lines* represent isobars; the *black arrows* represent the mean wind. The *shaded blue* area roughly outlines the dust-source region within the Syrian Desert.

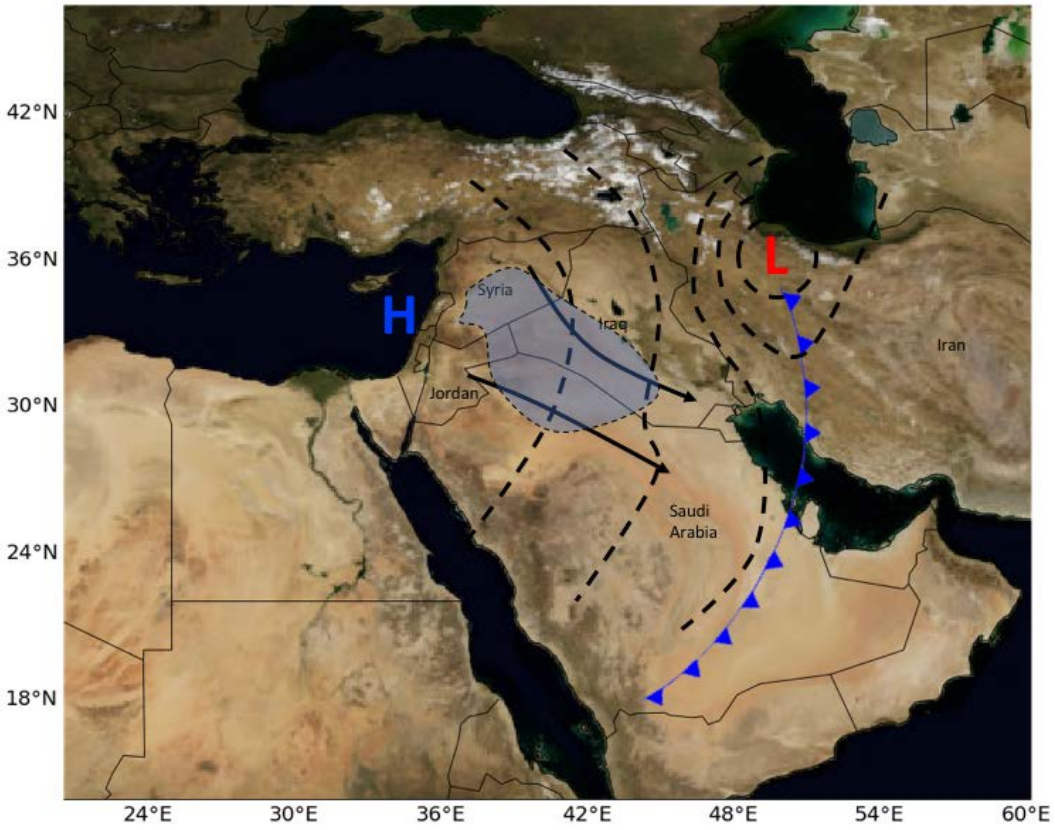

True-color and dust-enhanced MODIS Imagery from 1000 UTC 25 January 2010 suggests that dust originating in the Syrian Desert advected

downwind and covered most of southern Iraq and northeastern Saudi Arabia (Figure 3). The true-color MODIS image shows widespread cloud cover associated with the midlatitude cyclone responsible for the Shamal.

Figure 3. *Left*: MODIS true-color image showing the dust plume over the analysis region outlined in Fig. 1. *Right*: False-color dust-enhanced MODIS image (dust identified by the *pink* shading). Wind barbs show the CFSR 925 hPa winds valid at 1200 UTC on January 25 2010. MODIS imagery is valid at 1000 UTC on January 25 2010.

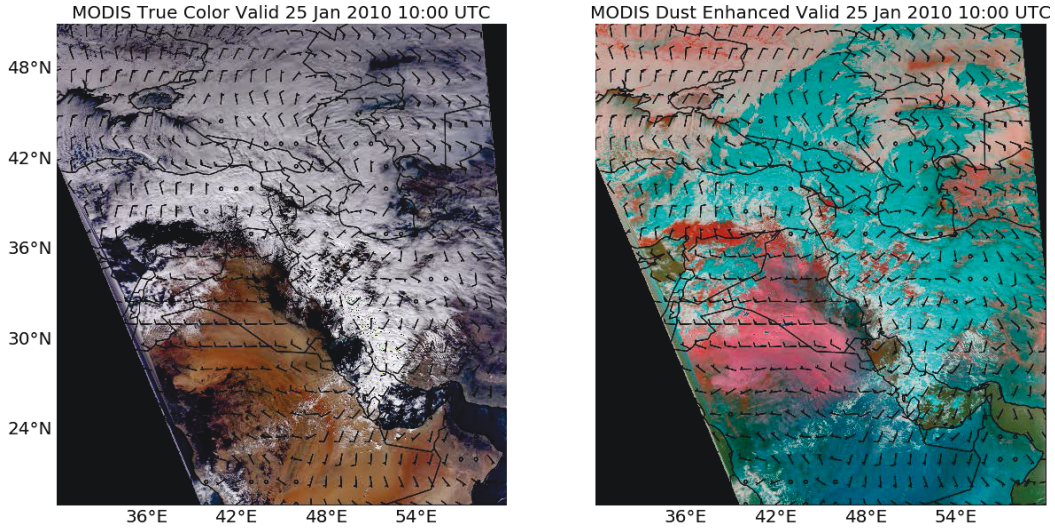

It is difficult to determine the southeastern-most extent of the dust-source region since any dust sources that may have been located underneath the dust plume were obscured by the plume itself in the satellite imagery.

According to the CFSR data, the synoptic evolution that led to this dust event began around 0000 UTC on January 24 when a mid-level synoptic-scale trough of low pressure started moving south across the Mediterranean Sea. A broad area of deeper southerly flow developed over the Greater Arabian Peninsula in response to the approaching system (Figure 4a). By 0000 UTC on 25 January, a cold front extending from a mid-level low pressure system had moved south across Iraq and Saudi Arabia (Figure 4b). At 1200 UTC on 25 January, the initial cold front was approximately located along the Iraq/Iran border, and westerly surface winds were present across much of the Arabian Peninsula (Figure 4c). During this period (2 hours after the timing of the Figure 3 MODIS images), the dust event was well underway. Blowing dust continued throughout the day on 25 January before waning in the evening as turbulence and lower atmospheric mixing abated from diurnal heat loss and winds shifted due to a second cold front approaching from the north (Figure 4d).

Figure 4. Annotated figures showing snapshots of 850 hPa temperature (*°C shaded*), 700 hPa geopotential height (*blue contours*), and 925 hPa wind barbs. Panels *a–d* show data from the CFSR, and panels *e–h* show data from the WRF-Chem simulation. *Red L's* indicate local minima in the 700 hPa geopotential height and represent the approximate location of the synoptic disturbance. The *thick black dashed lines* show the approximate location of a cold front associated with the Shamal.

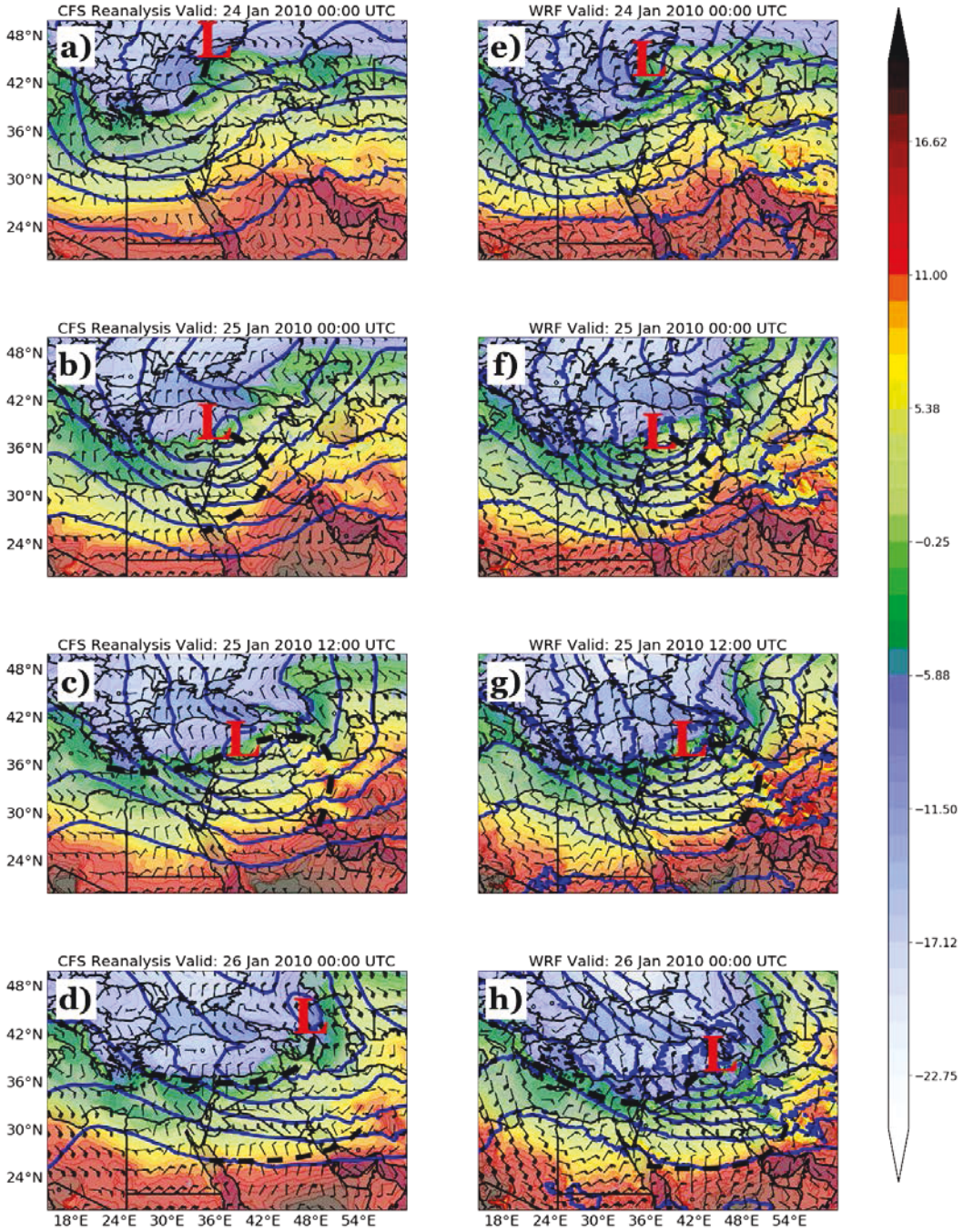

4.2 Overview of general meteorological conditions simulated by WRF-Chem

Because aerosol feedback capabilities were not switched on in the WRF-Chem model configuration, all three dust-event simulations evolved identical environmental conditions with the exception of dust concentrations. The configuration of WRF-Chem was able to adequately simulate the overall synoptic evolution of the event (Figure 4e–h). Model physics captured the southward motion of the midlatitude disturbance and the development and passage of both cold fronts and associated surface wind shifts related to the event. However, there were minor differences between the WRF-Chem simulations and the CFSR product with respect to the timing and intensity of each Frontal Passage (FROPA).

In the WRF-Chem version, both FROPAs occurred slightly earlier than in the reanalysis. For example, at 0000 UTC on 25 January, the frontal boundary in WRF-Chem was approximately located on the boarder of Iraq and Iran while the reanalysis product showed the boundary located over central Iraq (e.g., Figure 4b, f). Similarly, at 0000 UTC on 26 January, the second cold frontal boundary had pushed through Jordan to the northern border of Iraq in WRF-Chem but was located further north on the border of Jordan and Turkey in the reanalysis product. These timing differences could have affected simulated dust emission and transport throughout the event. In addition to minor timing differences, the WRF-Chem simulations also exhibited a generally stronger geopotential height gradient associated with the trough, indicating stronger lower tropospheric winds, which could also affect model dust emission and transport. While these disparities are mentionable, they are generally minor and likely affected dust emission and transport to a substantially lesser degree than the dust-emission parameterizations themselves.

To augment the evaluation of the WRF-Chem model, simulated Skew-T log-P diagrams were generated at locations indicated in Figure 1 and were compared to Skew-T log-P diagrams generated from radiosonde observations at these locations (Figure 5). From a broad perspective, the model was able to adequately simulate the atmospheric temperature, moisture, and wind profiles at both locations and both times; however, much of the fine-scale vertical variation was not simulated by WRF-Chem due to limitations in the model's vertical resolution and small-scale turbulence parameterizations. In particular, the agreement was remarkably good at

both locations on 25 January at 1200 UTC during the dust event, indicating that the meteorological forcing that drove the dust event was well-simulated by the WRF-Chem model.

Figure 5. Skew-T log-P diagrams shown for the OEMA (*top row*) and OERK (*bottom row*) locations in Fig. 1. *Red colors* indicate WRF-Chem simulated, and *black colors* indicate radiosonde observations. *Solid lines* represent temperature, and *dashed lines* represent dew point.

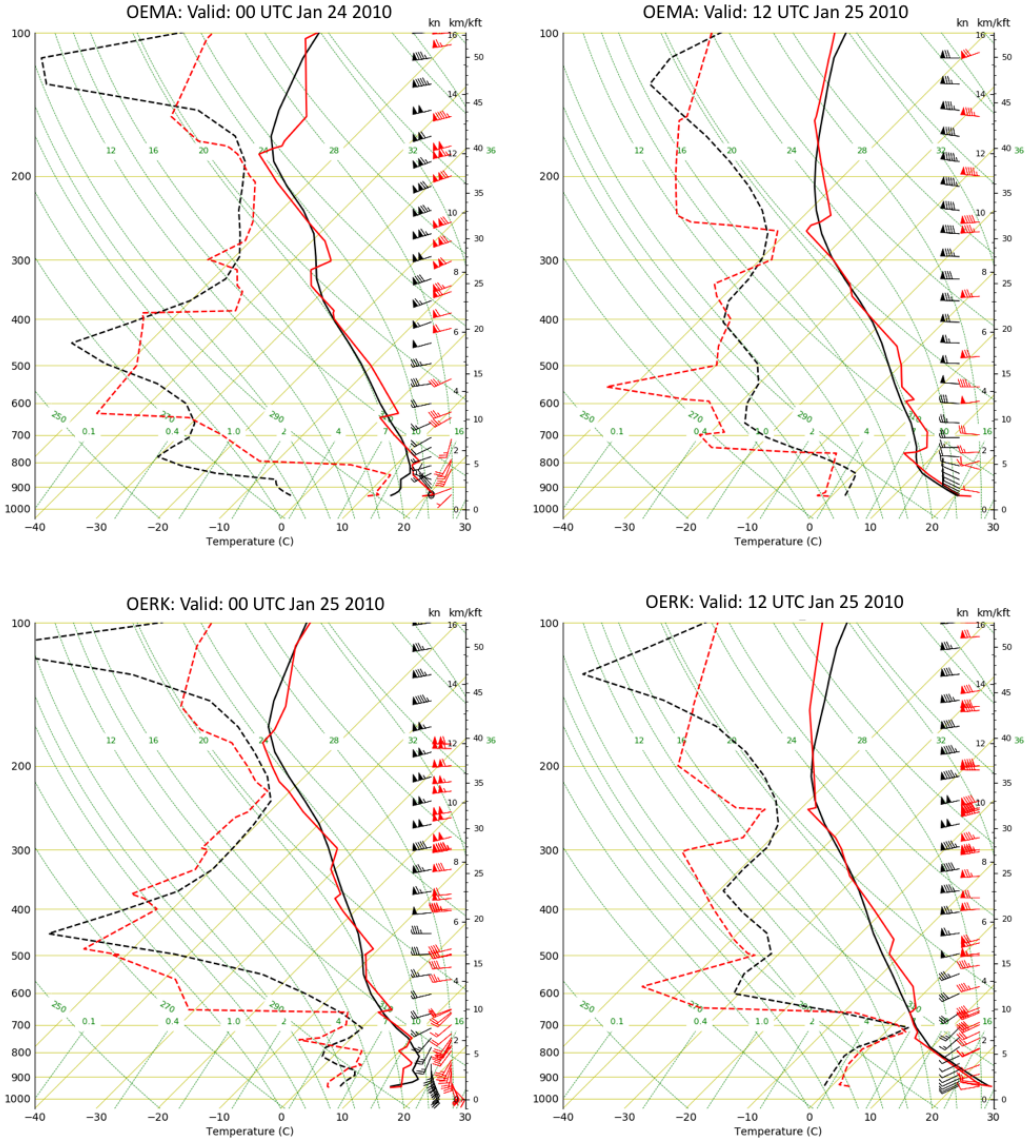

Overall, the model was able to adequately simulate the synoptic event that led to the dust storm over the Syrian Desert, suggesting that any major differences between observed and simulated atmospheric dust concentrations were most likely caused by deficiencies in the dust-source, emission, and deposition parameterizations rather than poorly simulated wind fields.

4.3 Comparison of dust-emission schemes

4.3.1 Qualitative comparison to satellite imagery

Figure 6 shows a qualitative spatial comparison between each dust scheme and the dust-enhanced MODIS image from 1000 UTC 25 January. In this figure, WRF-Chem–simulated cloud cover and AOD are colored to match the colors of clouds (cyan) and dust (pink) in the dust-enhanced image.

Figure 6. MODIS false-color image compared to model-simulated cloud cover (*cyan*) and AOD (*pink*). Valid for 1000 UTC 25 January 2010. Note that the color scales used in WRF-Chem are not quantitatively comparable to the MODIS imagery and are used only to aid in a qualitative spatial comparison between the satellite imagery and the model.

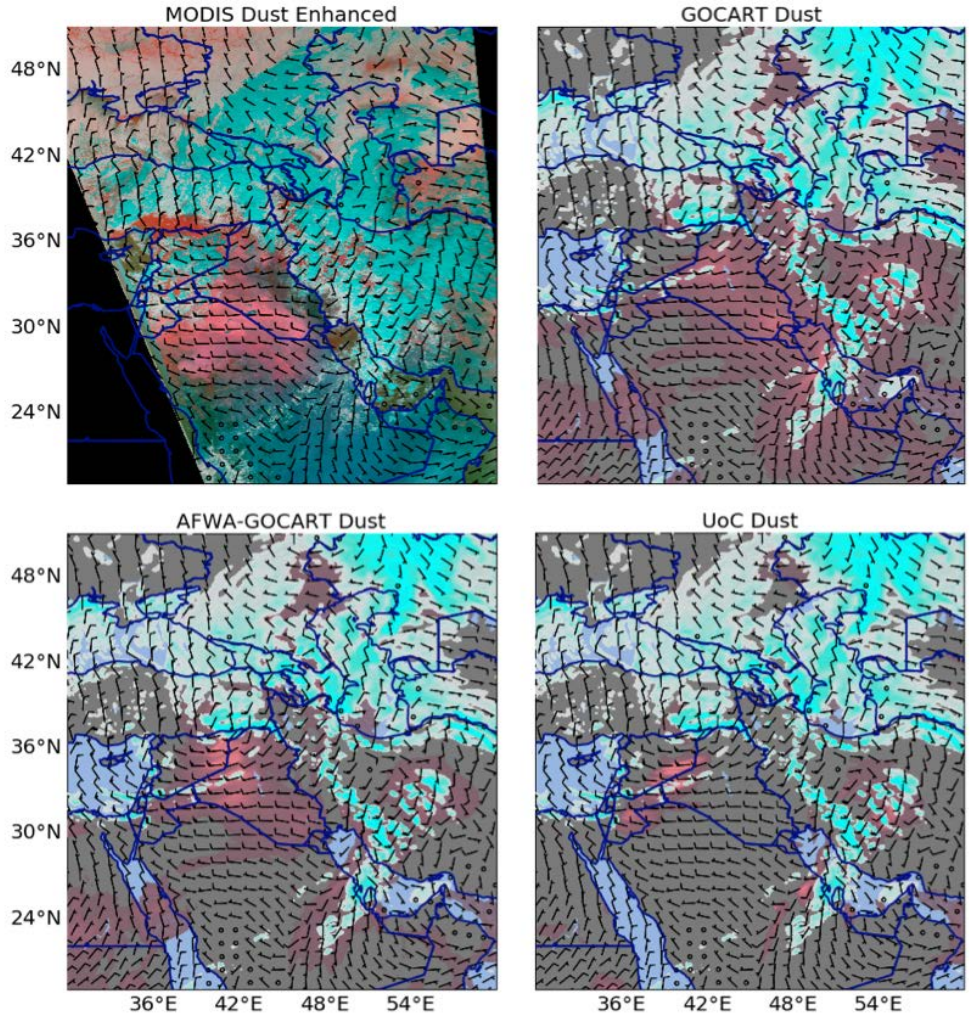

A few notable differences stand out in this comparison. In particular, the GOCART dust-emission scheme appears to generate a dust plume that is too expansive, covering all of Iraq, eastern Saudi Arabia, and most of Iran

(Figure 6b). While it is impossible to determine the extent of the actual dust plume over Iran and points further north and west due to extensive cloud cover, the absence of likely dust conditions (i.e., pink shading) in the satellite observations suggests that the large amounts of simulated dust in southeastern Saudi Arabia were erroneous (Figure 6a).

The AFWA dust-emission scheme produced plumes that aligned with the dust-enhanced MODIS image better than the GOCART dust-emission scheme. The simulated dust plume was concentrated over Iraq and roughly matched the location of the remotely sensed dust. The AFWA dust-emission scheme also produced less dust in southeast Saudi Arabia in the immediate vicinity of the initial cold front (Figure 6c). The UoC dust scheme largely failed to produce the observed dust plume, showing only a small area of dust along the Iraq/Jordan border and along the front in southeast Saudi Arabia.

All three dust parameterizations appeared to entirely miss the dust plume extension over northern Saudi Arabia. We speculate that this was because the model dust-source function, S, is zero over this region (e.g., Figure 1), thereby eliminating the possibility of dust emission over this area. It was unclear from the MODIS image if this error was due to issues in dust-source representation or a deficiency in how the WRF-Chem model handled dust deposition as the MODIS image only provides qualitative information about atmospheric dust conditions at a single date and time. Furthermore, it is unlikely that subjective dust-source identification methods (e.g., Walker et al. 2009; Sinclair and Jones 2017) would help for this case study due to the presence of clouds.

4.3.2 Comparison to observations

Figure 7 presents time series of 2 m temperature and 10 m wind speed and surface visibility generated using station observations and simulated WRF-Chem data.

The WRF-Chem simulations were able to replicate both the multiday downward trend in temperature associated with the initial FROPA and the diurnal cycle in temperature within about 2°–3°C at each station. Similarly, the surface winds were generally well represented at each station throughout the case study with the exception of the time period between 1200 and 1800 UTC on 25 January at the OERF surface observing station. We speculated that the observed surface winds may have been dominated

by turbulence or wind patterns generated by the local terrain that were not resolved by the model.

Figure 7. *Left panels*: Observed and simulated time series of 2 m temperature and 10 m wind speed for the OERF, OERR, OESK, and OETR stations marked in Fig. 1. *Green* colors show the WRF-Chem simulated variables, and *red* colors show the observed variables. *Right panels*: Observed and simulated time series of near-surface visibility. The *thick red line* indicates the observed visibility. Each *dashed line* indicates the model-simulated visibility from each of the three dust parameterizations (indicated by the legend in the uppermost panel). *Tan bars* mark times in which dust or blowing dust was reported in the surface observation.

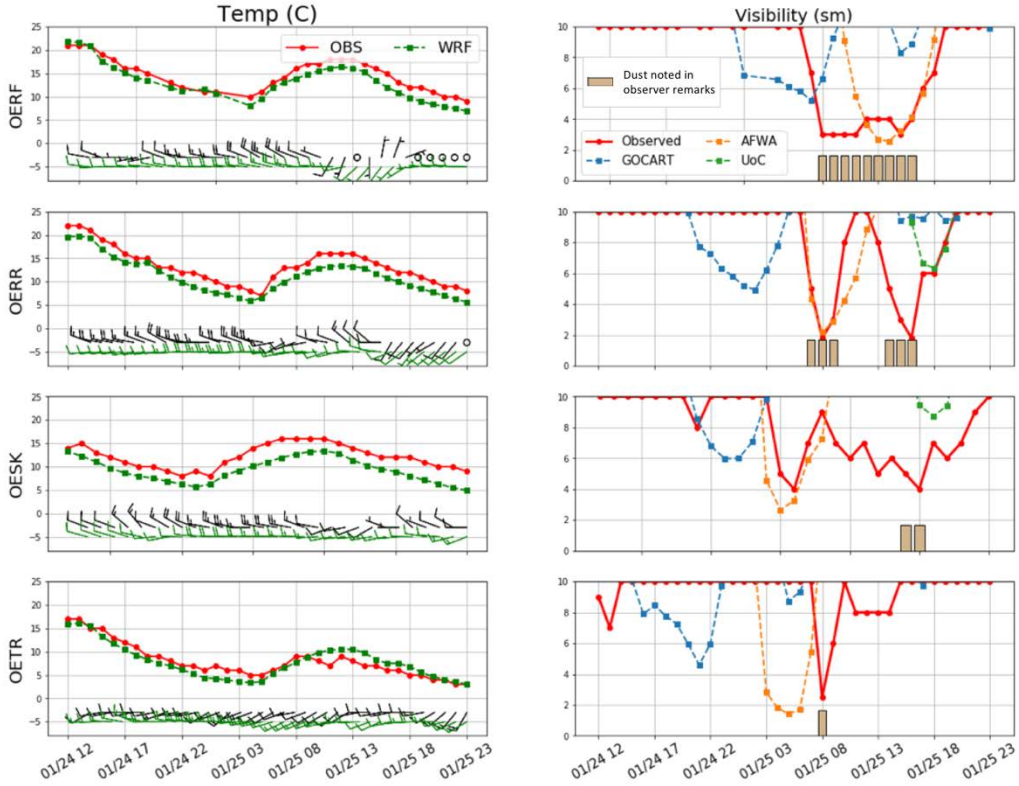

With respect to visibility, the AFWA dust-emission scheme generally performed better than the other two schemes and compared reasonably well to the observed visibility at three of the four stations. The relatively poor performance of the AFWA dust-emission scheme at the fourth station may have been because this station is located near the northwestern-most edge of the observed dust plume where minor differences in simulated timing and location of the event could have led to large errors at individual locations. The GOCART dust-emission scheme appeared to produce a dust-induced visibility reduction that is both too early and too weak compared to observations at all stations, and the UoC dust-emission scheme barely produced any dust-induced visibility reductions at any of the four station sites.

To investigate these differences in the dust concentrations, Figure 8 provides simulated snapshots of dust-emission fluxes produced using the various schemes. As expected, the simulation configured with the GOCART scheme had the most extensive footprint of dust emission, consistent with the most widespread dust plumes seen in Figure 6. The simulation configured with the AFWA scheme generally produced dust emission in the same general location of maximum dust emission produced by the GOCART scheme configuration, but overall emission flux magnitudes were lower and less widespread. In contrast, the simulation configured with the UoC scheme produced isolated, intense fluxes of dust over portions of Syria and Jordan with little dust emission elsewhere.

Figure 8. Comparison of dust vertical emission fluxes by mass for each dust parameterization for three times during the dust event.

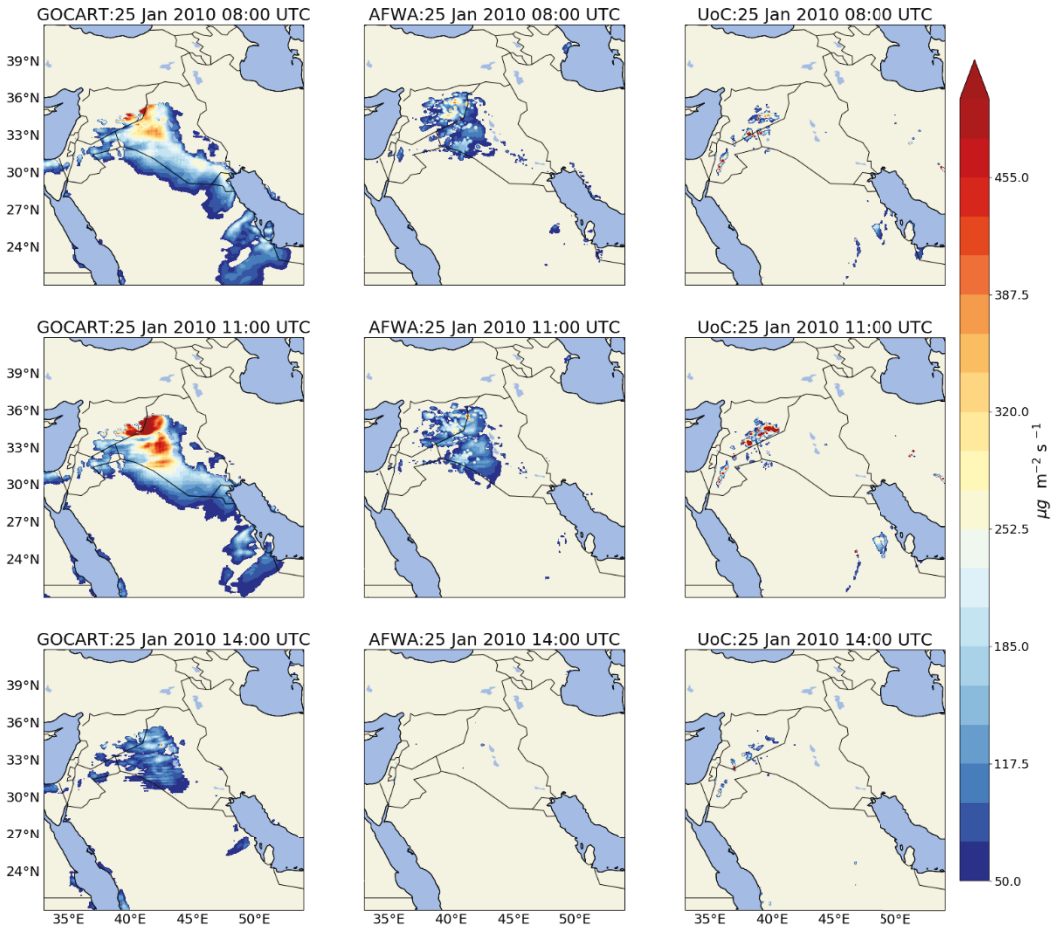

5 Extended Analysis and Discussion

Based on these brief analyses, there were indications that the WRF-Chem simulation configured with the AFWA dust-emission scheme performed better than the other two configurations for this particular case-study event. Though it is difficult and inappropriate to draw wholesale conclusions about model performance from a single case study with such a limited observational dataset, understanding why these simulations turned out so differently warrants further exploration.

The overly expansive footprint of dust emission in the GOCART scheme configuration was most likely due to the U_t calculation error. Large differences in magnitude between U and u^* effectively rendered simulated values of U_t to zero, dust-emission fluxes were proportional to U^3, and the only factors modifying emission rates were the S parameter and a conditional statement that ceased dust emission in areas where soil moisture values exceed 0.5 degrees of saturation.

Furthermore, we propose that the UoC scheme primarily failed to initiate the dust-emission activity near the Iraq/Saudi Arabia boarder because of a vegetation-based drag correction factor (r_c) applied in the u_{*t} calculation:

$$r_c = \left(\sqrt{1. - 0.5\lambda}\right)\left(\sqrt{1 + 100\lambda}\right), \tag{10}$$

where λ is a function of the vegetation fraction (c_f):

$$\lambda = 0.35 * \ln\left(1 - c_f\right) \tag{11}$$

Figure 9 illustrates the impact of the roughness correction, indicating that u_{*t} values were more than doubled by the drag correction factor in grid-cells with relatively low vegetation coverage (i.e., <15%). This correction factor affected the potential for dust emissions across a substantial portion of the region and, as a result, restricted dust emissions in northwestern Iraq. To illustrate this, we compared estimated saltation fluxes from the simulated friction velocity (u_*) following equation (8): one with the roughness correction applied to $u_{*,th}$ and one without the roughness correction applied to $u_{*,th}$ (Figure 10). This analysis indicated that the overall failure of the UoC scheme to reproduce the spatial extent of the observed dust plume could be largely attributed to the roughness correction factor applied to $u_{*,th}$. The expanded spatial extent of the saltation flux region in

Figure 10b suggests that absent the roughness correction, the UoC scheme would have likely been more similar to the AFWA scheme.

Overall, many of the model deficiencies with respect to dust emission are likely associated with a lack of good high-resolution data regarding dust sources and soil composition. For example, the dust-source function used in this study was developed for use in coarsely gridded (O(Δx) ~ 100 km) global atmospheric models, not high-resolution (e.g., Δx = 12 km) regional simulations. Furthermore, intrinsic soil properties that can substantially affect dust emission, such as plastic pressure or disaggregation potential, are poorly constrained for soils in the Middle East region, further increasing the uncertainty in dust emissions, particularly at fine scales.

Figure 9. Roughness correction factor as a function of the WRF-Chem vegetation fraction.

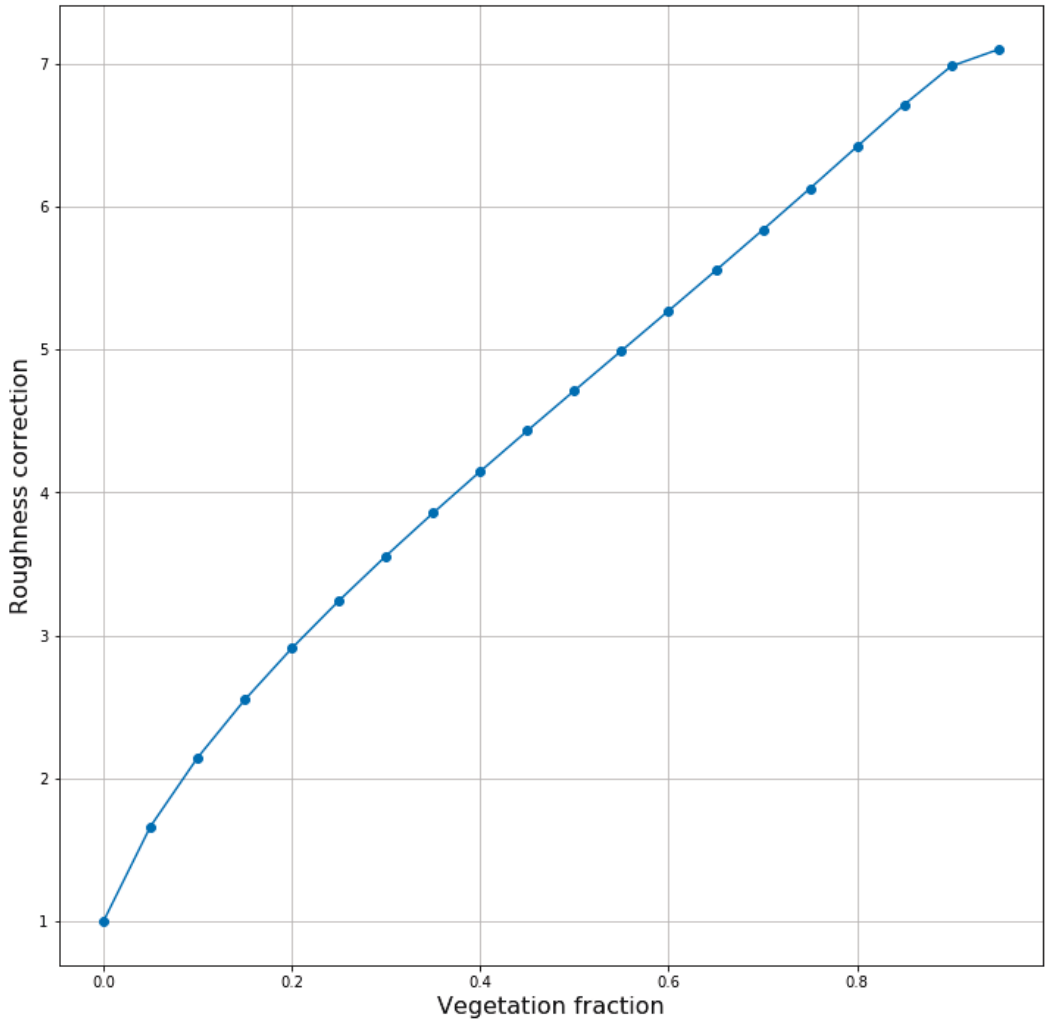

Figure 10. Theoretical saltation flux for a 60 µm diameter dust particle from the UoC parameterization. *Left*: $u_{*,th}$ includes the roughness correction. *Right*: $u_{*,t}$ does not include the roughness correction.

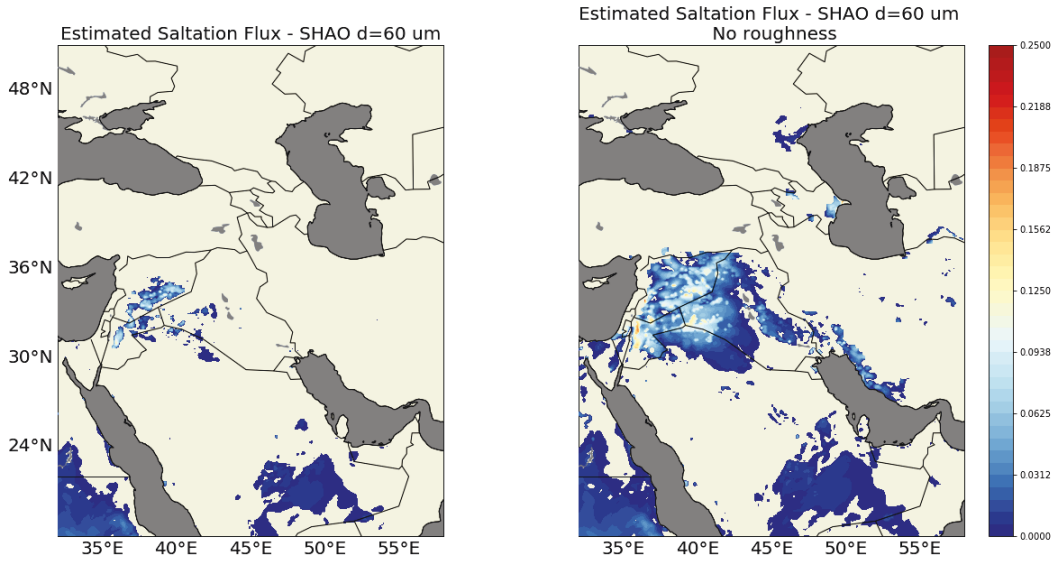

While these particular model simulations were able to simulate the meteorology behind the observed dust event, this was largely because this dust event was primarily driven by larger-scale synoptic forces (as opposed to convective-scale weather events like individual thunderstorms). The model will likely perform worse for convectively driven dust events because, while most properly configured NWP models can simulate convective activity with reasonable fidelity, the exact timing and location of individual convective events are likely to be wrong. These errors, combined with the aforementioned deficiencies in the underlying datasets that go into the dust flux parameterizations can severely degrade atmospheric dust prediction associated with convectively driven events.

6 Conclusions and Recommendations

In this report, we evaluated three different dust-emission parameterizations against observations for a dust storm case study over the Syrian Desert, which straddles the Iraq/Saudi Arabia border. We showed that the AFWA dust scheme performed the best out of the three as it was able to simulate the timing and extent of a large-scale dust plume and the variability in the dust-reduced visibility at four different surface stations with reasonable accuracy. In contrast, the GOCART dust scheme generated too broad a region of atmospheric dust, and the UoC dust scheme largely failed to produce any dust owing to a roughness correction factor that shut down dust production over most of the source region.

Our overall recommendation for individuals and agencies interested in NWP capabilities for dust, visibility, and air-quality applications is to use the AFWA dust-emission scheme when using WRF-Chem to simulate dust over the Middle East region, particularly in the winter months when surface attributes like loose particle availability and soil moisture strongly affect dust lofting potential. Furthermore, we recommend researchers focus on improving dust-source parameterizations better suited for high-resolution simulations and that efforts aimed at better constraining the intrinsic soil properties are continued.

References

Al-Hemoud, A., M. Al-Sudairawi, S. Neelamanai, A. Naseeb, and W. Behbehani. 2017. Socioeconomic Effect of Dust Storms in Kuwait. *Arabian Journal of Geosciences* 10:18.

Boucher, O., D. Randall, P. Artaxo, C. Bretherton, G. Feingold, P. Forster, V.-M. Kerminen, Y. Kondo, H. Liao, and U. Lohmann. 2013. Clouds and Aerosols. In *Climate Change 2013: The Physical Science Basis. Contribution of Working Group I to the Fifth Assessment Report of the Intergovernmental Panel on Climate Change*, 571–657. New York: Cambridge University Press.

Cavazos, C., M. C. Todd, and K. Schepanski. 2009. Numerical Model Simulation of the Saharan Dust Event of 6–11 March 2006 Using the Regional Climate Model Version 3 (RegCM3). *Journal of Geophysical Research: Atmospheres* 114 (D12): D12109.

Chin, M., D. L. Savoie, B. J. Huebert, A. R. Bandy, D. C. Thornton, T. S. Bates, P. K. Quinn, E. S. Saltzman, and W. J. De Bruyn. 2000. Atmospheric Sulfur Cycle Simulated in the Global Model GOCART: Comparison with Field Observations and Regional Budgets. *Journal of Geophysical Research: Atmospheres* 105 (D20): 24689–24712.

De Longueville, F., Y.-C. Hountondji, S. Henry, and P. Ozer. 2010. What Do We Know About Effects of Desert Dust on Air Quality and Human Health in West Africa Compared to Other Regions? *Science of the Total Environment* 409 (1): 1–8.

DeFries, R. S., and J. R. G. Townshend. 1994. Global Land Cover: Comparison of Ground-Based Data Sets to Classifications with AVHRR Data. In *Environmental Remote Sensing from Regional to Global Scales* 84–110. Chichester, UK: Wiley

Fécan, F., B. Marticorena, and G. Bergametti. 1998. Parametrization of the Increase of the Aeolian Erosion Threshold Wind Friction Velocity Due to Soil Moisture for Arid and Semi-Arid Areas. *Annales Geophysicae* 17 (1): 149–157).

14th Operational Weather Squadron. 2017. Climatic Snapshot Iraq [PowerPoint Slides] (17 October 2017). https://climate.af.mil (accessed 22 February 2017).

Freitas, S. R., K. M. Longo, M. F. Alonso, M. Pirre, V. Marecal, G. Grell, R. Stockler, R. F. Mello, and M. S. Gácita. 2011. PREP-CHEM-SRC-1.0: A Preprocessor of Trace Gas and Aerosol Emission Fields for Regional and Global Atmospheric Chemistry Models. *Geoscientific Model Development* 4 (2): 419–433.

Ginoux, P., M. Chin, I. Tegen, J. M. Prospero, B. Holben, O. Dubovik, and S.-J. Lin. 2001. Sources and Distributions of Dust Aerosols Simulated with the GOCART Model. *Journal of Geophysical Research: Atmospheres* 106 (D17): 20255–20273.

Ginoux, P., J. Prospero, O. Torres, and M. Chin. 2004. Long-Term Simulation of Global Dust Distribution with the GOCART Model: Correlation with North Atlantic Oscillation. *Environmental Modelling and Software* 19 (2): 113–128.

Grell, G. A., S. E. Peckham, R. Schmitz, S. A. McKeen, G. Frost, W. C. Skamarock, and B. Eder. 2005. Fully Coupled "Online" Chemistry within the WRF Model. *Atmospheric Environment* 39 (37): 6957–6975.

Jones, S. L. 2012. *Performance Assessment of WRF-Chem GOCART*. TR-SP-64. Offutt Air Force Base, NE: U.S. Air Force Weather Agency.

Horvath, H. 1971. On the Applicability of the Koschmieder Visibility Formula. *Atmospheric Environment* 5 (3): 177–184.

Knippertz, P., and J.-B. W. Stuut, ed. 2014. *Mineral Dust: A Key Player in the Earth System*. New York: Springer.

Kok, J. F. 2011. A Scaling Theory for the Size Distribution of Emitted Dust Aerosols Suggests Climate Models Underestimate the Size of the Global Dust Cycle. *Proceedings of the National Academy of Sciences* 108 (3): 1016–1021.

Kok, J. F., E. Parteli Jr., T. I. Michaels, and D. Bou Karam. 2012. The Physics of Wind-blown Sand and Dust. *Reports on Progress in Physics* 75 (10): 106901.

Kok, J. F., N. M. Mahowald, G. Fratini, J. A. Gillies, M. Ishizuka, J. F. Leys, M. Mikami, M.-S. Park, S.-U. Park, R. S. Van Pelt, and T. M. Zobeck. 2014. An Improved Dust Emission Model–Part 1: Model Description and Comparison Against Measurements. *Atmospheric Chemistry and Physics* 14 (23): 13023–13041.

Kumar, R., M. C. Barth, G. G. Pfister, M. Naja, and G. P. Brasseur. 2014. WRF-Chem Simulations of a Typical Pre-Monsoon Dust Storm in Northern India: Influences on Aerosol Optical Properties and Radiation Budget. *Atmospheric Chemistry and Physics* 14 (5): 2431–2446.

Liu, M., D. L. Westphal, S. Wang, A. Shimizu, N. Sugimoto, J. Zhou, and Y. Chen. 2003. A High-Resolution Numerical Study of the Asian Dust Storms of April 2001. *Journal of Geophysical Research: Atmospheres* 108 (D23):8653. doi:10.1029/2002JD003178.

Liu, M., D. L. Westphal, A. L. Walker, T. R. Holt, K. A. Richardson, and S. D. Miller. 2007. COAMPS Real-Time Dust Storm Forecasting during Operation Iraqi Freedom. *Weather and Forecasting* 22 (1): 192–206.

Mahowald, N. M., A. R. Baker, G. Bergametti, N. Brooks, R. A. Duce, T. D. Jickells, N. Kubilay, J. M. Prospero, and I. Tegen. 2005. Atmospheric Global Dust Cycle and Iron Inputs to the Ocean. *Global Biogeochemical Cycles* 19 (4): GB4025. doi:10.1029/2004GB002402.

Mahowald, N. M., J. A. Ballantine, J. Feddema, and N. Ramankutty. 2007. Global Trends in Visibility: Implications for Dust Sources. *Atmospheric Chemistry and Physics* 7 (12): 3309–3339.

Mahowald, N. M., S. Kloster, S. Engelstaedter, J. K. Moore, S. Mukhopadhyay, J. R. McConnell, S. Albani, S.C. Doney, A. Bhattacharya, M. A. J. Curran, M. G. Flanner, F. M. Hoffman, D. M. Lawrence, K. Lindsay, P.A. Mayewski, J. Neff, D. Rothenberg, E. Thomas, P.E. Thornton, and C. S. Zender. 2010. Observed 20th Century Desert Dust Variability: Impact on Climate and Biogeochemistry. *Atmospheric Chemistry and Physics* 10 (22): 10875–10893.

Mahowald, N., S. Albani, J. F. Kok, S. Engelstaeder, R. Scanza, D. S. Ward, and M. G. Flanner. 2014. The Size Distribution of Desert Dust Aerosols and Its Impact on the Earth System. *Aeolian Research* 15:53–71.

Marticorena, B., and G. Bergametti. 1995. Modeling the Atmospheric Dust Cycle: 1. Design of a Soil-Derived Dust Emission Scheme. *Journal of Geophysical Research: Atmospheres* 100 (D8): 16415–16430.

Middleton, N. J. 2017. Desert Dust Hazards: A Global Review. *Aeolian Research* 24:53–63.

Miller, S. D. 2003. A Consolidated Technique for Enhancing Desert Dust Storms with MODIS. *Geophysical Research Letters* 30 (20): 2071. doi:10.1029/2003GL018279.

National Centers for Environmental Prediction, National Weather Service, National Oceanic and Atmospheric Administration, and U.S. Department of Commerce. 2000, updated daily. *NCEP FNL Operational Model Global Tropospheric Analyses, continuing from July 1999*. Boulder, CO: Research Data Archive at the National Center for Atmospheric Research, Computational and Information Systems Laboratory. https://doi.org/10.5065/D6M043C6 (accessed October 2017).

Nickovic, S., G. Kallos, A. Papadopoulos, and O. Kakaliagou. 2001. A Model for Prediction of Desert Dust Cycle in the Atmosphere. *Journal of Geophysical Research: Atmospheres* 106 (D16): 18113–18129.

Okin, G. S., J. E. Bullard, R. L. Reynolds, J.-A. C. Ballantine, K. Schepanski, M. C. Todd, J. Belnap, M. C. Baddock, T. E. Gill, and M. E. Miller. 2011. Dust: Small-Scale Processes with Global Consequences. *EOS, Transactions American Geophysical Union* 92 (29): 241–248.

Peckham, S. E., J. Fast, R. Schmitz, G. A. Grell, W. I. Gustafson, S. A. McKeen, S. J. Ghan, R. Zaveri, R. C. Easter, and J. Barnard. 2011. *WRF/Chem Version 3.3 User's Guide*. NOAA Technical Memo. Boulder, CO, U.S. Department of Commerce, National Oceanic and Atmospheric Administration, Oceanic and Atmospheric Research Laboratories, Global Systems Division. https://ruc.noaa.gov/wrf/wrf-chem/Users_guide.pdf.

Prospero, J. M., P. Ginoux, O. Torres, S. E. Nicholson, and T. E. Gill. 2002. Environmental Characterization of Global Sources of Atmospheric Soil Dust Identified with the NIMBUS 7 Total Ozone Mapping Spectrometer (TOMS) Absorbing Aerosol Product. *Reviews of Geophysics* 40 (1): 1002.

Ravi, S., P. D'Odorico, D. D. Breshears, J. P. Field, A. S. Goudie, T. E. Huxman, J. Li, G. S. Okin, R. J. Swap, A. D. Thomas, S. Van Pelt, J. J. Whicker, and T. M. Zobeck. 2011. Aeolian Processes and the Biosphere. *Reviews of Geophysics* 49 (3): RG3001. doi:10.1029/2010RG000328.

Richter, D., and T. Gill. 2018. Challenges and Opportunities in Atmospheric Dust Emission, Chemistry, and Transport. *Bulletin of the American Meteorological Society*, in press. doi:10.1175/BAMS-D-18-0007.1.

Rizza, U., F. Barnaba, M. M. Miglietta, C. Mangia, L. Di Liberto, D. Dionisi, F. Costabile, F. Grasso, and G. Paolo Gobbi. 2017. WRF-Chem Model Simulations of a Dust Outbreak over the Central Mediterranean and Comparison with Multi-Sensor Desert Dust Observations. *Atmospheric Chemistry and Physics* 17 (1): 93–115.

Rushing, J. F., A. Harrison, and J. S. Tingle. 2005. *Evaluation of Application Methods and Products for Mitigating Dust for Lines-of-Communication and Base Camp Operations*. ERDC/GSL TR-05-9. Vicksburg, MS: U.S. Army Engineer Research and Development Center.

Saha, S., S. Moorthi, H.-L. Pan, X. Wu, J. Wang, S. Nadiga, P. Tripp, R. Kistler, J. Woollen, D. Behringer, and H. Liu. 2010a. The NCEP Climate Forecast System Reanalysis. *Bulletin of the American Meteorological Society* 91 (8): 1015–1057.

———. 2010b. *NCEP Climate Forecast System Reanalysis (CFSR) Monthly Products, January 1979 to December 2010*. Boulder, CO: Research Data Archive at the National Center for Atmospheric Research, Computational and Information Systems Laboratory. https://doi.org/10.5065/D6DN438J (accessed October 2017).

Shao, Y. 2001. A Model for Mineral Dust Emission. *Journal of Geophysical Research: Atmospheres* 106 (D17): 20239–20254.

———. 2004. Simplification of a Dust Emission Scheme and Comparison with Data. *Journal of Geophysical Research: Atmospheres* 109 (D10): D10202.

Shao, Y., J. F. Leys, G. H. McTainsh, and K. Tews. 2007. Numerical Simulation of the October 2002 Dust Event in Australia. *Journal of Geophysical Research: Atmospheres* 112 (D8): D08207.

Shao, Y., M. Ishizuka, M. Mikami, and J. F. Leys. 2011. Parameterization of Size-Resolved Dust Emission and Validation with Measurements. *Journal of Geophysical Research: Atmospheres* 116 (D8): D08203.

Shepherd, G., E. Terradellas, A. Baklanov, U. Kang, W. Sprigg, S. Nickovic, A. D. Boloorani, A. Al-Dousari, S. Basart, and A. Benedetti. 2016. *Global Assessment of Sand and Dust Storms*. Nairobi: United Nations Environment Programme.

Shinoda, M., J. A. Gillies, M. Mikami, and Y. Shao. 2011. Temperate Grasslands as a Dust Source: Knowledge, Uncertainties, and Challenges. *Aeolian Research* 3 (3): 271–293. doi: 10.1016/j.aeolia.2011.07.001.

Sinclair, S. N., and S. L. Jones. 2017. *Subjective Mapping of Dust Emission Sources by Using MODIS Imagery: Reproducibility Assessment*. ERDC/CRREL TR-17-8. Hanover, NH: U.S. Army Engineer Research and Development Center.

Sprigg, W. A., S. Nickovic, J. N. Galgiani, G. Pejanovic, S. Petkovic, M. Vujadinovic, A. Vukovic, M. Dacic, S. DiBiase, A. Prasad, and H. El-Askary. 2014. Regional Dust Storm Modeling for Health Services: The Case of Valley Fever. *Aeolian Research* 14:53–73.

Tegen, I., and I. Fung. 1994. Modeling of Mineral Dust in the Atmosphere: Sources, Transport, and Optical Thickness. *Journal of Geophysical Research: Atmospheres* 99 (D11): 22897–22914.

Walker, A. L., M. Liu, S. D. Miller, K. A. Richardson, and D. L. Westphal. 2009. Development of a Dust Source Database for Mesoscale Forecasting in Southwest Asia. *Journal of Geophysical Research: Atmospheres* 114 (D18): D18207.

Wang, F., X. Zhao, C. Gerlein-Safdi, Y. Mu, D. Wang, and Q. Lu. 2017. Global Sources, Emissions, Transport and Deposition of Dust and Sand and Their Effects on the Climate and Environment: A Review. *Frontiers of Environmental Science and Engineering* 11 (1): 13. doi:10.1007/s11783-017-0904-z.

Webb, N. P., A. Chappell, C. L. Strong, S. K. Marx, and G. H. McTainsh. 2012. The Significance of Carbon-Enriched Dust for Global Carbon Accounting. *Global Change Biology* 18 (11): 3275–3278.

Webb, N. P., J. E. Herrick, J. W. Van Zee, E. M. Courtright, C. H. Hugenholtz, T. M. Zobeck, G. S. Okin, T. E. Barchyn, B. J. Billings, R. Boyd, S. D. Clingan, B. F. Cooper, M. C. Duniway, J. D. Derner, F. A. Fox, K. M. Havstad, P. Heilman, V. LaPlante, N. A. Ludwig, L. J. Metz, M. A. Nearing, M. L. Norfleet, F. B. Pierson, M. A. Sanderson, B. S. Sharratt, J. L. Steiner, J. Tatarko, N. H. Tedela, D. Toledo, R. S. Unnasch, R. S. Van Pelt, L. Wagner. 2016. The National Wind Erosion Research Network: Building a Standardized Long-Term Data Resource for Aeolian Research, Modeling and Land Management. *Aeolian Research 22*:23–36.

Westphal, D. L., C. A. Curtis, M. Liu, and A. L. Walker. 2009. Operational Aerosol and Dust Storm Forecasting. IOP Conference Series: *Earth and Environmental Science 7* (1): 012007.

Woodward, S. 2001. Modeling the Atmospheric Life Cycle and Radiative Impact of Mineral Dust in the Hadley Centre Climate Model. *Journal of Geophysical Research* 106 (D16): 18155–18166.

REPORT DOCUMENTATION PAGE

Form Approved
OMB No. 0704-0188

1. REPORT DATE *(DD-MM-YYYY)*	2. REPORT TYPE	3. DATES COVERED *(From - To)*
August 2018	Technical Report/Final	

4. TITLE AND SUBTITLE

A Comparison of Simulated Dust Produced by Three Dust-Emission Schemes in WRF-Chem: Case-Study Assessment

5a. CONTRACT NUMBER

5b. GRANT NUMBER

5c. PROGRAM ELEMENT NUMBER
053HJ0/FAN U4357509

6. AUTHOR(S)

Theodore W. Letcher and Sandra L. LeGrand

5d. PROJECT NUMBER

5e. TASK NUMBER

5f. WORK UNIT NUMBER

7. PERFORMING ORGANIZATION NAME(S) AND ADDRESS(ES)

U.S. Army Engineer Research and Development Center (ERDC)
Cold Regions Research and Engineering Laboratory (CRREL)
72 Lyme Road
Hanover, NH 03755-1290

8. PERFORMING ORGANIZATION REPORT NUMBER

ERDC/CRREL TR-18-13

9. SPONSORING / MONITORING AGENCY NAME(S) AND ADDRESS(ES)

Assistant Secretary of the Army for Acquisition, Logistics, and Technology
103 Army Pentagon
Washington, DC 20314-1000

10. SPONSOR/MONITOR'S ACRONYM(S)

11. SPONSOR/MONITOR'S REPORT NUMBER(S)

12. DISTRIBUTION / AVAILABILITY STATEMENT

Approved for public release; distribution is unlimited.

13. SUPPLEMENTARY NOTES

ERDC 6.2 Geospatial Research and Engineering (GRE) ARTEMIS STO-R DUST-CLOUD

14. ABSTRACT

Airborne mineral dust is one of the main forms of atmospheric aerosols, influencing, among other things, global weather patterns, biogeochemical processes, air quality, sensor performance, and visibility conditions on the ground. This study evaluates three dust-emission parameterizations available in the widely used Weather Research and Forecast model: the GOCART (Global Ozone Chemistry Aerosol Radiation and Transport), AFWA (Air Force Weather Agency), and UoC (University of Cologne) dust-emission schemes. The simulations were performed for a dust event that occurred over the Arabian Peninsula on 25 January 2010. The simulations were able to adequately reproduce the meteorological conditions of the event, and all three dust-emission schemes produced a dust event over the Arabian Peninsula. However, there were large differences in magnitude and extent between the three emissions schemes. Of the three schemes evaluated here, the AFWA scheme most closely matched the observed dust plume. Analysis revealed that differences between the schemes could largely be traced to differences in how each calculate the threshold wind speed (i.e., the minimum wind speed required for dust to be lofted).

15. SUBJECT TERMS

Air quality, Climate, Computer simulation, Dust, Dust storms, Geospatial data, Weather

16. SECURITY CLASSIFICATION OF:			17. LIMITATION OF ABSTRACT	18. NUMBER OF PAGES	19a. NAME OF RESPONSIBLE PERSON
a. REPORT	b. ABSTRACT	c. THIS PAGE			19b. TELEPHONE NUMBER *(include area code)*
Unclassified	Unclassified	Unclassified	SAR	41	